Corrosion behavior of cold sprayed 7075Al composite coating reinforced with TiB2 nanoparticles

Xinliang Xie, Bilel Hosni, Chaoyue Chen, Hongjian Wu, Yuelin Li, Zhe Chen, Christophe Verdy, Omar E I Kedim, Qingdong Zhong, Ahmed Addad, et al.

Corrosion behavior of a cold sprayed 7075Al composite coating reinforced with TiB_2 nanoparticles

Xinliang Xie[1, 2*], Bilel Hosni[3], Chaoyue, Chen[4], Hongjian Wu[1], Yuelin Li[4], Zhe Chen[5], Christophe Verdy[1], Omar EI Kedim[3], Qingdong Zhong[4], Ahmed Addad[2], Christian Coddet[1], Gang JI[2*], Hanlin Liao[1]

1. ICB UMR 6303, CNRS, Univ. Bourgogne Franche-Comté, UTBM, F-90010 Belfort, France
2. Univ. Lille, CNRS, INRAE, Centrale Lille, UMR 8207 - UMET - Unité Matériaux et Transformations, F-59000 Lille, France
3. FCLAB Research Federation (FR CNRS 3539), 90010 Belfort Cedex, France
4. Shanghai University & State Key Laboratory of Advanced Special Steel, 149 Yanchang Road, Shanghai 200072, P.R. China
5. State Key Laboratory of Metal Matrix Composites, Shanghai Jiao Tong University, Shanghai 200240, China

Abstract: Cold spray (CS), as a novel surface treatment technique, has been widely used for repairing damaged components and as protecting coatings, especially for the applications of aircraft and marine components. To further improve the mechanical properties, while maintaining the corrosion resistance of pure Al and Al alloy coatings, ceramic particles are commonly added into the Al matrix to produce particle-strengthened Al matrix composite (P-AMC) coatings. In this study, dense 7075Al composite coatings reinforced with uniformly distributed in-situ TiB_2 nanoparticles (hereafter named TiB_2/7075Al) were successfully produced by CS using a gas-atomized composite powder and the propulsive gases of air and helium. Following this, the corrosion behavior of the cold sprayed (CSed) TiB_2/7075Al composites was investigated using Tafel polarization, electrochemical impedance, spectroscopy, and immersion tests in 0.1 M and 0.6 M NaCl solutions, and were compared to those of the CSed pure 7075Al coating and bulk 7075Al-T6 material. Electrochemical tests revealed that the composite coating exhibits a higher corrosion rate than the pure 7075Al coating, primarily caused by a galvanic coupling between TiB_2 nanoparticles and the more active Al matrix. Compared to the air-processed coatings, the He-processed ones exhibit higher densities of defects, like dislocations, and precipitates due to larger plastic deformation of the sprayed particles, which result in more active sites for corrosion and thus lower corrosion

resistance. Low-temperature annealing treatment (230 °C/6h) reduces these defects to increase the corrosion resistance of the CSed coatings. Comparatively, high-temperature annealing treatment (412 ℃/4h) results in coarsening of precipitates and grain growth to increase the corrosion rate of the coatings. Corrosion mechanisms of the CSed and annealed composite coatings related to the microstructure evolution were investigated in detail.

Keywords: Particle reinforced Al matrix composites; Cold spraying; TiB_2 reinforcement; Aqueous corrosion

1. Introduction

Surface treatment techniques such as cold spray (CS), along with other thermal spray processes, are commonly used for depositing a coating being protective of the metallic substrate material [1-4]. The principle of CS process is that feedstock powder particles are accelerated to supersonic velocity through a naval nozzle by highly compressed gas (e.g. air, N_2, and He); plastic deformation of the particles during impact with the substrate surface or previously deposited layer leads to the formation of either a mechanical interlocking or metallurgical bonding [5-9]. In this process, particle/particle and particle/substrate bonding are obtained relying on the kinetic energy (plastic deformation) instead of heat energy (melting), which is different from other thermal spray processes (e.g. atmosphere plasma spraying, high-velocity oxygen fuel spraying). As a result, residual thermal stresses, oxidation, and unexpected phase transformation of as-sprayed coatings could be minimized or eliminated [10-13]. Moreover, extensive plastic deformation of the sprayed particles often leads to a fully dense coating with good adhesion. These features make CS suitable for repairing damaged parts and depositing corrosion/wear-resistant coatings. Recently, a variety of cold sprayed (CSed) metals (Al, Ti, Ta, Ni …), alloys, and composite coatings have been investigated for corrosion protection [14-21].

Pure Al or Al alloy coatings have been for a long time considered as a good corrosion protection solution in atmospheric and aqueous environments thanks to the formation of a very thin and almost impervious aluminum oxide layer [22]. Thus, it is not surprising that several studies [19, 23-27] have been conducted on corrosion protection of metallic parts using CSed Al or Al alloys. For instance, Karthikeyan *et al.* [22] investigated the electrochemical properties of the AA1100 coatings CSed onto an AA1100 substrate using pure He and He-20 vol.% N_2

mixture as the propulsive gases. They claimed that such coatings exhibit better corrosion resistance than the AA1100 substrate. Nevertheless, pure He processed coatings had higher hardness but inferior corrosion resistance in comparison to the one processed with He-20 vol.% N_2 due to greater particle deformation. Similarly, it was reported by Tao *et al.* [25] that the CSed pure Al coatings exhibit better corrosion resistance than the bulk pure Al sample in a neutral solution. On the contrary, Ngaia *et al.* [19] studied the corrosion behavior of CSed 7075Al coatings prepared using He and N_2 as spraying gases. They found that the N_2-processed sample exhibited worse corrosion resistance than the He-processed sample due to the limited particle deformation and high porosity level when using N_2 as the propellant gas. Therefore, the porosity and plastic deformation degree take an important role in determining the corrosion performance of the CSed pure Al coatings. Nevertheless, the effect of plastic deformation degree on the corrosion behavior seems still unclear which needs further investigation.

Although deposition of pure Al or Al alloy coatings can improve the corrosion performance of metallic components, they are not stiff enough to protect the substrate against mechanical damages during service [18, 21, 28]. Regarding this, previous studies demonstrated that the addition of hard ceramic reinforcements into the Al matrix to produce particle strengthened Al matrix composites (P-AMCs) can effectively improve their mechanical properties without sacrificing too much its corrosion resistance [29-31]. In general, the improved properties include a higher density, enhanced microhardness, and tribological performance as well as bonding strength in CSed coatings due to enhanced hammering and strengthening effects of the reinforcement particles [32, 33]. As summarized in Table 1, the CSed Al matrix composite coatings were deposited onto different substrates (i.e. Mg alloys or steels) for corrosion protection. When Al-based coating is deposited onto steel, it acts as the anode [23]. In this case, the chemical composition and microstructure of the coating are the dominative factors for the corrosion resistance. On the other hand, when the Al-based coating is sprayed onto Mg alloys, it acts as the cathode [34]. In most of these cases, the through-thickness pores will govern the corrosion rate. However, adding ceramic reinforcement particles into the Al matrix via CS could lead to distinct corrosion behavior. Irissou *et al.* [11] claimed that Al-Al_2O_3 composite coatings exhibit similar corrosion resistance compared to the unreinforced pure Al coating. Tao *et al.* [35] and Spencer *et al.* [36] found out that the addition of α-Al_2O_3 into the Al matrix has little

effect on its protection ability. Da Silva et al. [23] even reported that Al-Al_2O_3 composite coatings exhibit a slightly better corrosion resistance than the pure Al coatings due to the decreased active area in the composite coating as a result of the partial replacement of the Al matrix by Al_2O_3 particles. Wang *et al.* [37] also revealed that the Al5056-SiC composite coatings offer better corrosion resistance than the unreinforced Al5056 coating, while the SiC content has little effect on the corrosion behavior. Quite the reverse, according to the investigations of Meydanoglu *et al.* [18], the addition of ceramic particles increases corrosion rate of 7075 Al coatings since the enhanced plastic deformation provides more numerous active sites for corrosion in comparison with the unreinforced 7075Al coatings. Furthermore, the investigation of the CSed Al-$Mg_{17}Al_{12}$ composite coating revealed that the bonding condition between Al splats and $Mg_{17}Al_{12}$ particles plays an important role in determining its corrosion performance [38]. It was found that a high strain rate located at inter-particle boundaries provides preferential sites for pitting or galvanic corrosion, particularly when a high degree of defects are located in these regions [27]. It can also be learned from the literature that the type of ceramic particles could affect the corrosion behavior of AMCs [18, 39, 40]. In general, SiC and Al_2O_3 particles are the two most commonly used reinforcements for anti-corrosion AMC coatings due to their neutral property [41, 42]. Besides, some other ceramic particles (e.g. B_4C) are also used as reinforcements for AMC coatings. Therefore, the corrosion behavior of CSed composite coatings should be closely related to porosity, microstructure, type of reinforcement particles, and interactions between the Al matrix and reinforcement particles.

Different from the above-mentioned composite coatings produced only from powder mixtures, this study made a step forward to use a gas-atomized AlZnMgCu (7075Al) composite powder reinforced with in-situ TiB_2 nanoparticles as the new feedstock material for CS. As the TiB_2 particles are in-situ formed in the 7075Al matrix by a chemical reaction inside the liquid phase before atomization, it was recently demonstrated that the reinforcement of microhardness and tensile strength was achieved by combing the microstructural features of the homogenous distribution of TiB_2 nanoparticles, refined matrix grain size and tightly-bonded TiB_2/Al interface [43]. However, the assessment of corrosion behavior in such a composite coating is necessary before potential applications can be proposed. Therefore, this first objective of this study aimed to investigate the influence of adding in-situ nano-sized TiB_2 particles into the

7075Al matrix on the corrosion behavior of the composite coating. The second one aimed to reveal the influence of particle deformation as well as post-annealing treatments on the corrosion behavior of CSed pure 7075Al and TiB_2/7075Al composite coatings. Corrosion properties were evaluated using electrochemical measurements (potentiodynamic and potentiostatic curves) and immersion tests. Detailed analysis of the microstructure evolution was conducted to reveal corrosion mechanisms of the as-sprayed and annealed coatings.

Table 1 Summary of the corrosion behavior of the CSed P-AMCs

Materials	Main processing parameters	Substrate material	Ceramic particle size, μm	Ceramic particles content in powders, vol.%	Corrosion test conditions	Corrosion behavior	Reference
Al-αAl_2O_3	Air, P_g =1.6 MPa T_g=230 ℃	AZ91D Mg alloy	1-30	25, 50	3.5 wt.% NaCl solution	Adding α-Al_2O_3 has no negative impact on corrosion resistance of the composite coatings	[35]
Al-Al_2O_3	N_2, P_g =0.62MPa T_g=500 ℃	Mild steel and 7075Al	25.5	10, 30, 50, 75	3.5 wt.% NaCl solution	Composite coatings exhibited similar saltwater corrosion resistance compared to the pure Al coating.	[11]
Al-Al_2O_3 6061Al-Al_2O_3	He, P_g 0.62 MPa T_g=125 ℃	AZ91E Mg alloy	20	25, 50, 75	5 wt % NaCl solution	Neither the Al_2O_3 volume fraction nor annealing treatment can remarkably affect the corrosion behavior of the coatings.	[36]
5056Al-SiC	Air, P_g =2.6 MPa T_g=600 ℃	Al	48-92.6	15, 30, 60	0.1M Na_2SO_4 solution	Better corrosion resistance was obtained in the SiC strengthened composite coating, while the SiC content has little effect on its corrosion performance.	[37, 44]
7075-SiC 7075Al-B_4C	He, P_g= 0.98 MPa Tg=300 ℃	T6 6061 Al alloy	28 7	20	3.5 wt.% NaCl solution	The addition of SiC or B_4C particles increased the corrosion rate of the 7075Al composite coating.	[18]
Al-$Mg_{17}Al_{12}$	He, P_g =0.98 MPa Tg=300 ℃	AZ91D Mg alloy	48.5	50, 70	3.5 wt.% NaCl solution	The corrosion resistance of the composite coating was reduced when the $Mg_{17}Al_{12}$ particles were added into the Al matrix	[38]
Al-Al_2O_3/Al	N_2, P_g =2.5 MPa T_g=350 ℃	Low carbon steel	2-180	25	5 wt % NaCl solution	Slightly better corrosion resistance was obtained in the composite coating versus the unreinforced pure Al coating.	[23]
Al-Al_2O_3	He, P_g 0.62 MPa T_g=125 ℃	AZ91 Mg alloy	20	25, 50, 75	3.5 wt% NaCl solution	Corrosion potentials are lower than the bulk CP Al	[32]
Al_2O_3-2024Al	P_g 0.7-0.9 MPa T_g=400-600 ℃	Al2024-T3	15-50	20, 40, 60 wt.%	3.5 wt% NaCl solution	Al 2024-20 wt.% Al_2O_3 composite coating showed the best corrosion performance.	[45]

2. Experimental details

2.1 Fabrication of composite powder

The TiB_2/7075Al composite powder was fabricated by two steps using in-situ chemical reaction of reactive salts in the melted Al alloys followed by gas-atomization. First, the TiB_2 nanoparticles were introduced through a chemical reaction between the salts of K_2TiF_6 and KBF_4 ($3K_2TiF_6+6KBF_4+10Al \rightarrow 9KAlF_4+K_3AlF_6+3TiB_2$) in melted pure Al at around 900 ℃. A suitable amount of pure Zn, Mg, and Al-Cu master alloys (99.99%, CHALCO, China) were then added and homogenized for 10 min to transform TiB_2/Al to TiB_2/7075Al composite. Second, conventional gas atomization with N_2 was used to acquire the composite powder. Chemical composition of the composite powder was 5.4 wt.% Zn, 1.5wt.% Cu, 2.4 wt.% Mg, 7.0 wt.% TiB_2 (~4.2 vol.%) with Al balance, based on the measurement of inductively coupled plasma atomic emission analysis (ICP-AES). More details about the in-situ composite powder production can be found in Ref. [46]. The sieved atomized powder with the particle size in the range of 25-57 μm was used for CS. A pure 7075Al powder (LERMPS, France) atomized and sieved in the same conditions was also used as the feedstock for the sake of comparison.

2.2 Cold spray deposition and post-annealing processes

To evaluate the influence of processing parameters on coating microstructure and corrosion performance, CS deposition was carried out on 7075Al-T6 plate substrates (CHALCO, China) using two different processing conditions. In order to enhance the adhesion between the substrate and coating, surface of the substrate was sand-blasted using alumina grits prior to spraying (ISO 6344, Grit designation, P100). The main CS processing parameters used in this study are listed in Table 2. In the first condition (hereafter referred to C1), powders were deposited using CGT 3000 gun with a homemade CS system (LERMPS, UTBM, France). Compressed air and argon were used as the propellent and carrier gases, respectively. The nozzle inlet pressure and temperature were set to 3.0 MPa and 550°C, respectively. The SiC nozzle was water-cooled to prevent clogging. In the second condition (hereafter referred to C2), He gas with a nozzle inlet pressure of 1.8 MPa, and a temperature of 320°C was employed to accelerate the powder particles using a homemade He circulation CS system (LERMPS, UTBM, France). A polymer nozzle with an expansion ratio of 14.0 was installed in this CS system. More details about this specific CS system can be found in Ref. [47]. Further, in both C1 and C2 conditions, a standoff distance of 30 mm and a traverse speed of 100 mm/s was used. 20

passes were carried out to produce thick coatings (~2 mm). The 7075Al-T6 plate substrate material is referred to as ‘bulk 7075Al’.

Table 2 Main process parameters used for coating deposition.

Conditions	Nozzle material	Propellant gas	Carrier gas	Gas pressure (MPa)	Gas temperature (°C)	CS system
C1	SiC	Air	Ar	3.0	550 °C	CGT-3000
C2	Polymer	He	He	1.8	320 °C	LERMPS

In order to investigate the influence of post-heat treatment on the corrosion performance of the CSed coatings, the C2 coatings (both the pure 7075Al and TiB_2/7075Al composite) were annealed under an argon atmosphere using a homemade furnace (LERMPS, France) at a low temperature of 230 °C for 6h and a high temperature 412 °C for 4h, which hereafter referred as HT1 and HT2, respectively. They were followed by slow cooling within the furnace down to the room temperature. Based on the previous literature [48, 49], HT1 was selected for the release of residual stress without evident grain growth, while HT2 was a commonly used annealing procedure for 7075Al alloy, which may have remarkable grain growth and inter-splat boundary enhancement. All these factors would affect the finial corrosion performance of the CSed coatings.

2.3 Microstructural characterization

XRD examination was carried out to further identify the residual lattice strain evolution during annealing treatment using an X-ray diffractometer (Siemens D5000, Germany) with the Co ($\lambda = 1.78897$ Å) source at the current of 40 mA, voltage of 35 kV and scan step of 0.004°.

Feedstock powders and CSed coatings were characterized using a scanning electron microscope (SEM) equipped with energy-dispersive spectroscopy [50] unit (JSM5800LV, JEOL, Japan). The porosity level of each as-sprayed coating was estimated by analyzing five cross-sectional images from digital optical micrographs using ImageJ software (ImageJ, NIH, Bethesda, Md.). The same method was also used to measure the average number ratio and average area fraction of the pits or caves in the corroded surface of the samples. Two transmission electron microscopes (TEM), both operated at 200 kV and equipped with EDS

units, were used for fine characterization (FEI Tecnai G2 and FEI Titan Themis 300, USA). Cross-sectional TEM samples were prepared by mechanical polishing and final ion milling using a Gatan Model 691 precision ion polishing system.

2.4 Electrochemical measurements

Corrosion behavior of the CSed and annealed coating samples, as well as bulk 7075Al, were assessed using Tafel polarization, electrochemical impedance spectroscopy (EIS) and immersion tests in NaCl solutions. Prior to each corrosion experiment, specimens were mounted in epoxy resin with an effective square area of about 1 cm^2 being exposed to the corrosive medium. All the samples were mechanically polished till the use of a fine abrasive alumina paper (2000 grit).

Immersion experiments were conducted in 0.1M and 0.6 M NaCl solutions, in open circuit condition for 7 days at room temperature. After immersion tests, samples were cleaned using deionized water and observed by SEM. Potentiodynamic polarization measurements were performed in 0.1 M and 0.6 M NaCl solutions using using an EC-Lab V10.12 system (BioLogic, France). Three-electrode electrolyte cell with a saturated calomel electrode (SCE) as the reference and Pt foil as the counter electrode was used for all the measurements. The solution was purged with argon for 15 min before the tests were started and it purged with argon during the whole tests. After the samples were maintained for 5 min in the testing cell with the NaCl solution to permit electrode stabilization, potentiodynamic polarization curves were recorded by applying a potential voltage from -1.25 V to +0.5 V at a scan rate of 0.167 mV/s. EIS measurements were conducted by immersing the samples in the 0.6 M NaCl solution with a potentiostatic mode at open circuit potential (OCP) with a sinusoidal AC perturbation of 10 mv (rms) amplitude in the frequency range 100 kHz to 1 Hz. EIS measurements were conducted using Shanghai Chenhua Chi660 Electrochemical workstation (CH Instruments Inc, China), followed by analysis of the spectra with the ZSimpWin software (AMETEK, USA). At least two tests were conducted for each condition to confirm the validity of all the electrochemical measurements.

3. Results

3.1 Microstructure characterization

3.1.1 Microstructure of the feedstock powders

The SEM micrographs of the as-received 7075Al and TiB_2/7075Al composite powders are shown in Fig. 1a and d, respectively. Both powders present a nearly spherical shape and have similar particle size distributions (D_{10}=17 μm, D_{50}=35 μm, D_{90}=63 μm for the pure 7075Al powder and D_{10}=18 μm, D_{50}=37 μm, D_{90}=67 μm for the composite powder). Besides, some satellite-like fine particles are attached to the large particles, which likely result from the small melt droplets clinging to the surface of large droplets during gas atomization. The cross-sectional micrographs of the initial particles are shown in Figs. 1b and e. The pure 7075Al particle interior exhibits a dendritic microstructure with the evident contrast showing the dendritic α-Al cores (grey) and boundaries (greyish white). Recent study of M.R. Rokni *et al.* [51] has identified the Mg $(Zn, Al, Cu)_2$ phase in the as-atomized 7075Al powder. The composite particle exhibits equiaxed microstructure with an average grain size of about 1.5 μm (Fig. 1f), being two times smaller than that of the pure 7075Al particle (~3 μm). The in-situ formed TiB_2 reinforcement particles with the size ranging from a few hundred nanometers to a few microns appear uniformly distributed inside the composite particle. With the limited spatial resolution of SEM, the majority of nanosized TiB_2 particles are largely invisible but were confirmed by our previous papers [46, 52].

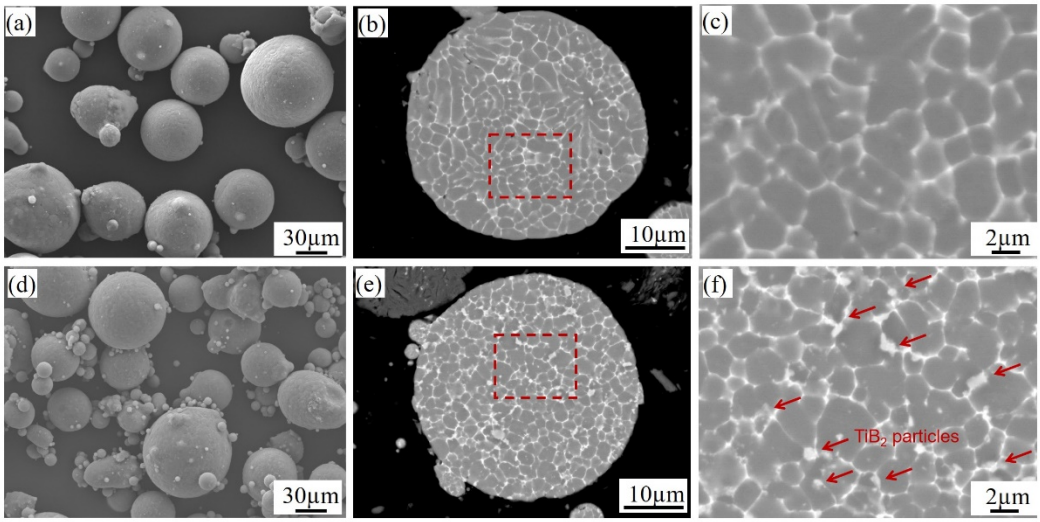

Fig. 1 SEM images showing (a, d) particle morphologies and (b, e) cross-sectional BSE

micrographs of the (a-c) pure 7075Al and (d-f) TiB_2/7075Al composite powders. (e) and (f) are the magnified views of the corresponding regions in (b) and (e).

3.1.2 Microstructure of the as-sprayed coatings

The representative cross-sectional microstructure of the pure 7075Al C1 coating shown in Fig. 2a reveals a relatively dense structure with deformed particles well bonded with each other. Some small pores (average porosity of 0.68± 0.04%) are locally present at the junctions of the deformed particles, resulting from insufficient deformation of the initially spherical powder particles. Besides, it can be noted that the initial grain structure of the feedstock powder was largely maintained, and only the particle boundaries were heavily deformed. Thus, the particles experience significantly more plastic strain at their border than in the center. Observation made perpendicularly to the surface (Fig. 2a), reveals a slightly higher degree of plastic deformation of particles in the direction of an impact than in parallel to the surface (Fig. 2b).

The composite coating (Fig. 2c and d) seems denser than the pure 7075Al coating (Fig. 2a and b) with only a few small pores being observed at the junctions of the deformed particles. This is confirmed by average porosity values of 0.49 ± 0.03% and 0.68 ± 0.04% for the TiB_2/7075Al-C1 composite sample and pure 7075Al-C1 sample, respectively. That decrease in porosity could be attributed to the enhanced peening effect [35, 53] if one considers that the deposition efficiency of the composite (~27 %) is lower than that of pure 7075Al (~38 %). The addition of TiB_2 particles into the 7075Al matrix increases its microhardness, and thus a higher critical velocity is required for deposition. As more composite particles rebound off the coating surface owing to unsuccessful bonding, the enhanced in-situ shot peening effect produced by these rebound particles can further deform the previously deposited layers [16, 53, 54]. Thus, it may be assumed that enhanced peening occurs for the composite as more particles rebound owing to unsuccessful bonding. Therefore, besides a uniform TiB_2 particles distribution within the coating, a denser structure is obtained for the composite versus pure 7075 Al.

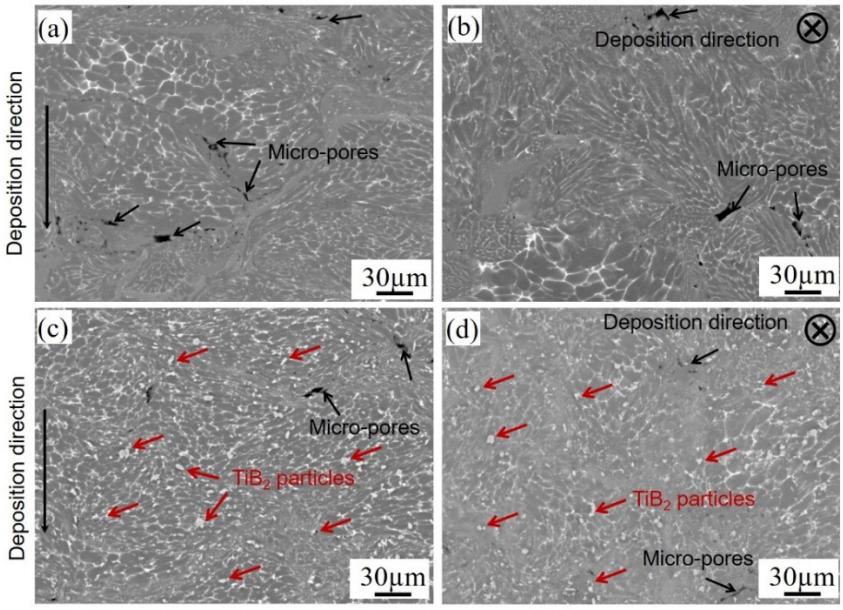

Fig. 2 BSE/SEM images showing the microstructure of the (a, b) 7075Al and (c, d) TiB_2/7075Al composite coatings produced by C1: (a) and (c) cross-sectional views; (b) and (d) top views.

The representative cross-sectional microstructure of the pure 7075Al-C2 coating (Figs. 3a and b) reveals a fully dense structure with very few visible sub-micron pores. Similarly, the TiB_2/7075Al composite coating (Figs. 3c and d) exhibits a lower porosity level (0.15± 0.02%) than the pure 7075Al coating (0.24±0.02%). Both the top-surface and cross-sectional views display a similar microstructure with largely deformed particles (Fig. 3). The enhanced plastic deformation is attributed to the fact that a much higher particle impact velocity upon CS deposition can be obtained when using He as the propellant gas as compared to the compressed air due to its lower gas molecular weight, which causes better gas flow acceleration through de-Laval nozzle [55, 56]. In comparison with the microstructure obtained at C1, the particles in C2 deposits are deformed so severely that their boundary regions exhibit a refined network of intermetallic phases. A similar microstructure was reported in a He-sprayed 7075Al coating by Ngai *et al.* [19].

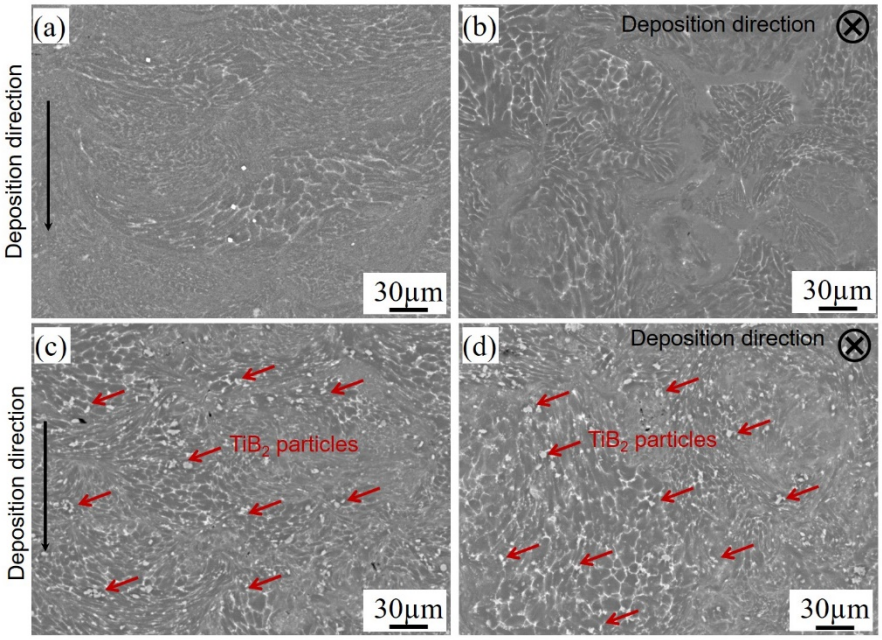

Fig. 3 BSE/SEM micrographs of the microstructure of the (a, b) 7075Al and (c, d) TiB_2/7075Al composite coatings produced by C2: (a) and (c) cross-sectional views; (b) and (d) top views.

TEM images in Fig. 4 show the cross-sectional micrographs of the TiB_2/7075Al-C2 composite coating with a partial overview of two adjacent particles in Fig. 4a. Along with the bonded interface, some voids remain (Fig. 4a), indicating a lack of metallic bonding in these regions. Magnified views of this interfacial region are shown in Fig. 4c and d. A large number of dislocation networks are visible inside the deformed grains (particle 1) together with nano-sized equiaxed grains (or subgrains). Zou *et al.* [57] and Kang *et al.* [58] indicate that these refined and equiaxed grains of approximatively 200 nm in size are formed by dynamic recrystallization due to high plastic deformation of the particles at their boundaries. As shown in Fig. 4e, this highly deformed region exhibits a typical lamellar structure, with the elongation direction perpendicular to the deposition direction. The magnified view in Fig. 4f shows a number of needle-like precipitates in the lamellar grains. Precipitates nucleated at the grain boundaries (GBs) have larger size and irregular shape, which may be attributed to early heterogeneous nucleation followed by accelerated growth due to GB diffusion. However, the needle-like ultrafine precipitates inside the elongated grains may result from dynamic and static precipitation under high strain levels during deposition [59]. EDS elemental maps in Fig. 5 show that most of the precipitates are composed of Al, Zn, Mg, and Cu elements. According to

previous studies [51, 60], these precipitates are likely Mg(Zn, Cu, Al)$_2$ phase. Moreover, as marked by the red arrows in Fig. 4e and f, the nano-sized TiB_2 particles are mainly dispersed at the GBs and appear as well bonded to the Al matrix.

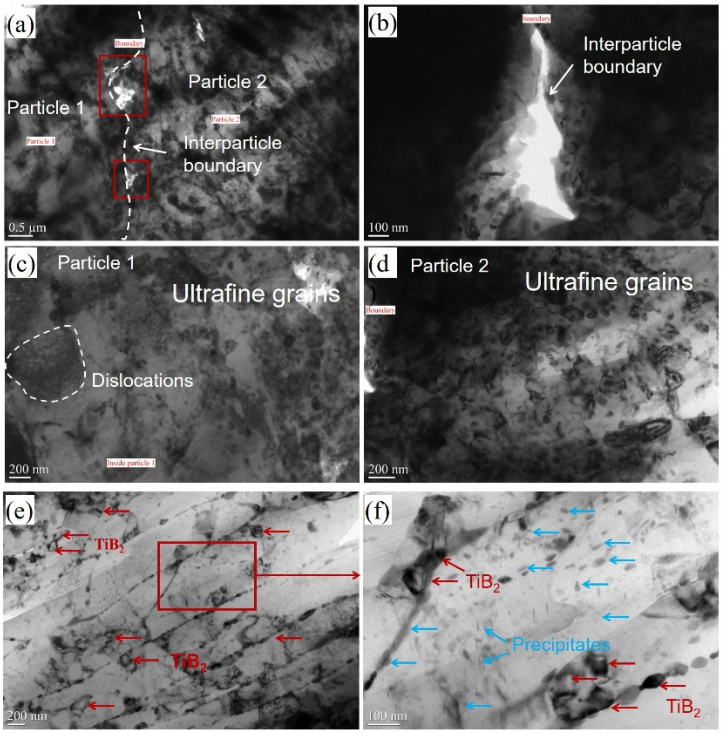

Fig. 4 TEM images showing the microstructure of the TiB_2/7075Al-C2 sample in different regions: (a) interfacial zone between two particles; (b) magnified micrograph of the interface; (c) and (d) ultrafine grain structure of particle 1 and particle 2 near the interface; (e) highly deformed grains with laminar structure; (f) magnified area of (e) showing nano-sized precipitates and TiB_2 particles in the Al matrix.

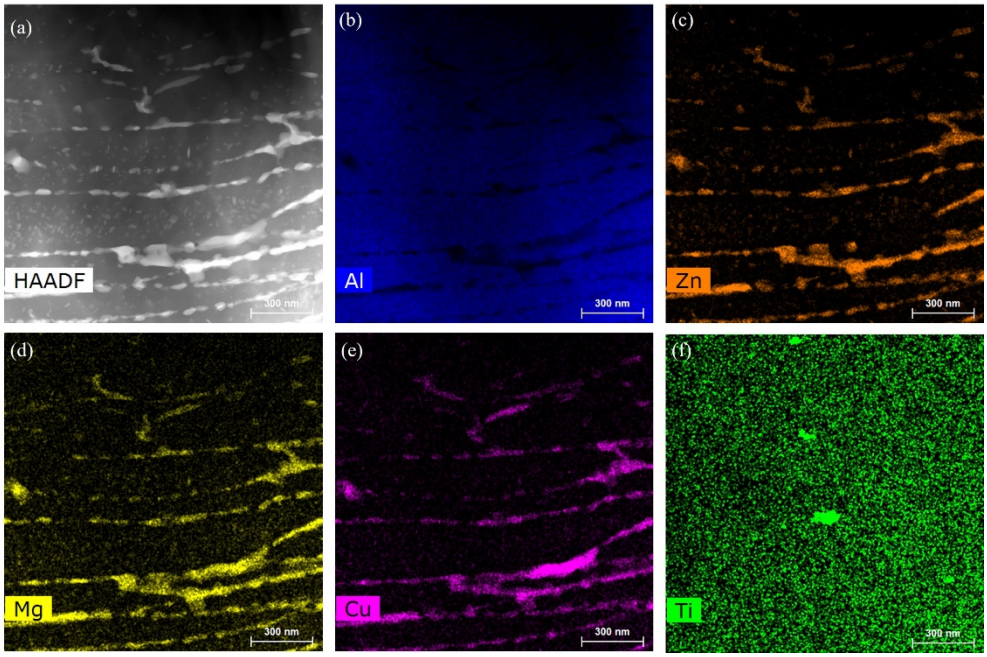

Fig. 5 TEM/EDS mapping of the TiB_2/7075Al-C2 sample showing the distribution of Al, Zn, Mg, Cu, and Ti elements.

3.1.3 Microstructure of the post annealed coatings

Fig. 6 shows BSE/SEM cross-sectional micrographs of the C2 coatings after annealing treatment using different conditions. The microstructure of the HT1 samples in Fig. 6a and b exhibit a similar grain size compared to the as-sprayed C2 samples. The inter-splat boundaries become obscurely compared to the as-sprayed state. Moreover, a variety of white precipitates are observed in the highly deformed interparticle regions. The white precipitates should originate from the growth of the precipitates after low-temperature treatment. After HT2 treatment, remarkable grain growth can be seen from the SEM images (Fig. 6c and d) for both the pure 7075Al and TiB_2/7075Al composite coatings. In this case, the inter-splat interfaces are disappeared as a result of prominent atom diffusion at the higher annealing temperature. Moreover, some individual white precipitates are distributed in the matrix of the HT2 samples. Therefore, it is also reasonable to speculate that these precipitates could derive from the coarsening of the nanosized precipitates observed in the as-sprayed state (see Fig. 4 and Fig. 5) during annealing treatment.

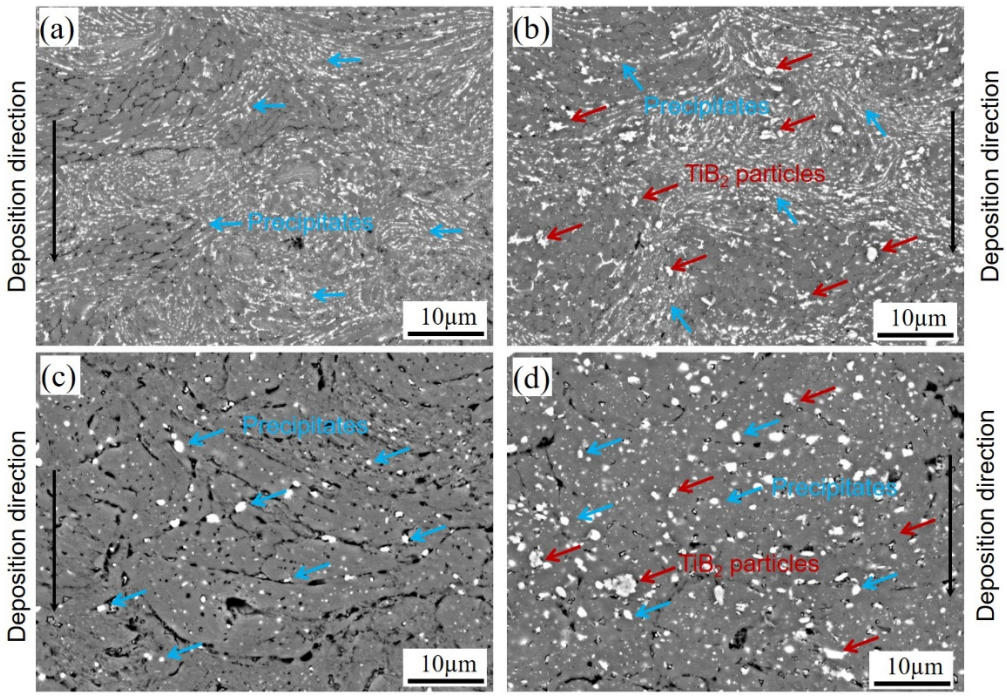

Fig. 6 BSE/SEM images of the annealed 7075Al-C2 and TiB_2/7075Al-C2 composite deposits at different conditions: (a) 7075Al-C2-HT1; (b) TiB_2/7075Al-C2-HT1; (c) 7075Al-C2-HT2; (d) TiB_2/7075Al-C2-HT2.

3.2 Corrosion behavior of the as-sprayed and post annealed coatings

3.2.1 Immersion studies

Surface morphologies of the 7075Al bulk, 7075Al coatings, and TiB_2/7075Al composite coatings before and after immersion in either 0.1 M or 0.6 M NaCl solution for 7 days are shown in Fig. 7. Contrary to the relatively smooth surface of the bulk 7075Al, the CSed coatings show sharp scratches resulting from sample preparation.

After immersion in a 0.1 M NaCl solution for 7 days, scratches on the surface of the bulk 7075Al material become obscurely (Fig. 7b) indicating the occurrence of general corrosion during immersion. Some signs of local corrosion (small pits) are also observed on the surface. After immersion in a 0.6 M NaCl solution for 7 days, more severe local corrosion appears on the surface.

After 7 days of immersion of the 7075Al-C1 coating in 0.1 M NaCl for 7 days, scratches have disappeared and some individual pits are seen on the corroded surface (Fig. 7e). Pits are commonly observed for 7075Al alloy immersed in the NaCl solutions [19, 61]. When immersed

in 0.6 M NaCl for 7 days, large and irregular shaped pits, even caves (with a diameter of 100 to 300 μm) are observed on the corroded surface (Fig. 7f). Around these large pits, there are many corrosion products, which are most likely oxides or hydroxides. These pits probably originate from the anodic dissolution of the matrix around the second phase particles sitting at the GB. As corrosion proceeds and the matrix gradually dissolves, these pits become larger and larger and finally form the irregular shaped caves. For the 7075Al-C2 coating, observations are similar, and it can be furthermore noted that NaCl concentration does not change much the features. The cross-sectional morphologies of the corroded 7075Al-C2 sample in Fig. 8 show deep caves with the crevices initiated and propagated primarily along with the interparticle interface. The statistical results of the pits on the corroded surface of the samples are given in Table 3. The results imply that pit seems easy to form in the CSed pure 7075Al coating, especially for the C2 samples immersed in a solution with higher chloride concentration.

The TiB_2/7075Al-C1 composite coatings display a different corrosion behavior. After immersion in 0.1 M NaCl for 7 days, scratches are still visible on the corroded surface (Fig. 7h). Meanwhile, no sign of pits can be observed. Instead, a thin oxide film is formed on the corroded surface after immersion, which can protect the surface from corrosion. When the solution concentration is increased to 0.6 M, fewer scratches can be observed, and a few pits also appear. Observations are similar for the TiB_2/7075Al-C2 coating although pitting seems a little bit more pronounced. The statistical results of the pits in Table 3 reveal a significant reduction in both pits number and volume fraction for the TiB_2/7075Al composite coating compared to the pure 7075Al coating. The cross-sectional morphologies of the TiB_2/7075Al-C2 composite sample in Fig. 8c and d also prove these observations. Nevertheless, large pits or caves are not formed, indicating a better corrosion resistance of the composite coatings in static conditions than that of the pure 7075 coatings.

Fig. 9 shows the corroded surface morphologies of the annealed samples after 7 days of immersion in 0.6 M NaCl solution. It can be noted that pits are also present on the corroded surfaces of both the pure 7075Al-C2-HT1 and TiB_2/7075Al-C2-HT1 composite samples (Fig. 9a and b). According to the statistical results in Table 3, the HT1 annealed samples exhibit fewer pits or caves than the as-sprayed C2 samples. The cross-sectional morphology of the HT1

annealed samples in Fig. 10a shows large and deep caves, which is similar to the observation of the as-sprayed pure 7075Al sample. The magnified image in Fig. 10b also displays that the crevices initiate and propagate along with the interparticle interface. As can be seen in Fig. 10c and d, the HT1 composite sample exhibits similar corroded morphologies as the as-sprayed state.

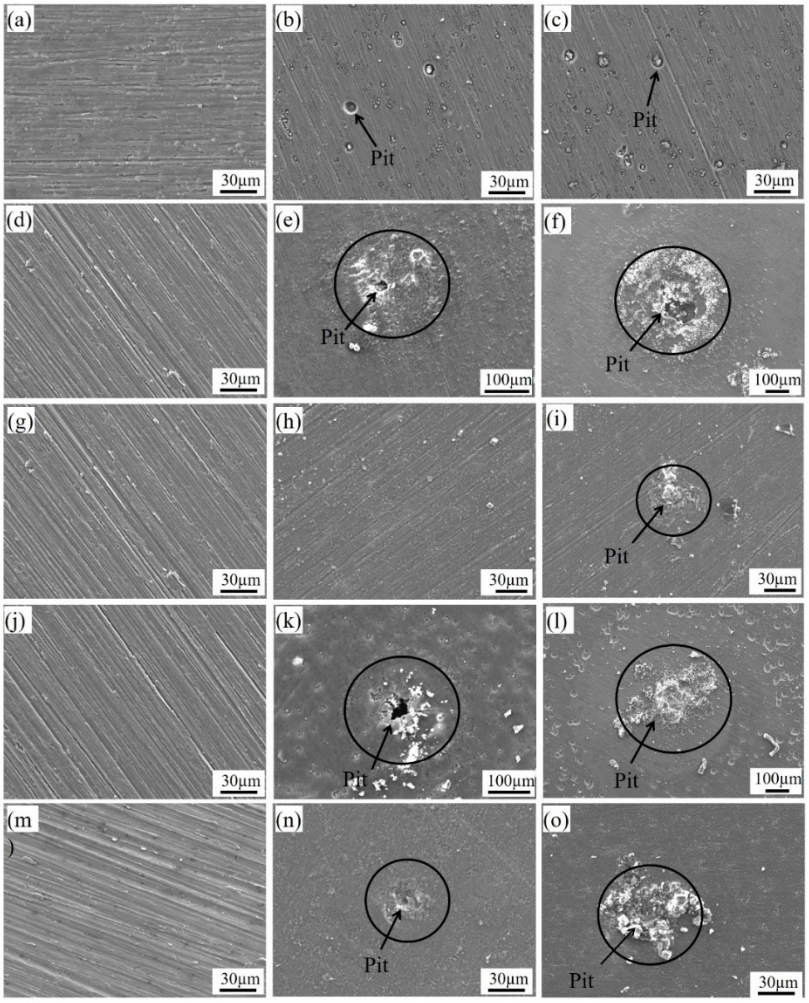

Fig. 7 SEM images of the 7075Al bulk, 7075 Al and TiB_2/7075Al composite coatings before (first row) and after immersion in 0.1 M (middle row) and 0.6 M (third row) NaCl for 7 days: (a-c) 7075Al bulk; (d-f) 7075Al-C1; (g-i) TiB_2/7075Al-C1; (j-l) 7075Al-C2; (m-o) TiB_2/7075Al-C2.

Different corroded morphologies are observed for the HT2 samples (Fig. 9c and d). As for the pure 7075Al sample, both uniform corrosion morphology and pits are present on the corroded surface. A similar observation is found on the cross section of the 7075Al-C2-HT2

samples (see Fig. 10e). However, the presence of white particles (containing oxygen and chlorine) beneath the coating surface (see Fig. 10f) suggests that the corrosive media has passed through the surface film into the interior of the composite coating. Prominent pits and uniform corrosion can be seen in the composite sample, indicating a higher annealing temperature treatment results in worse corrosion resistance.

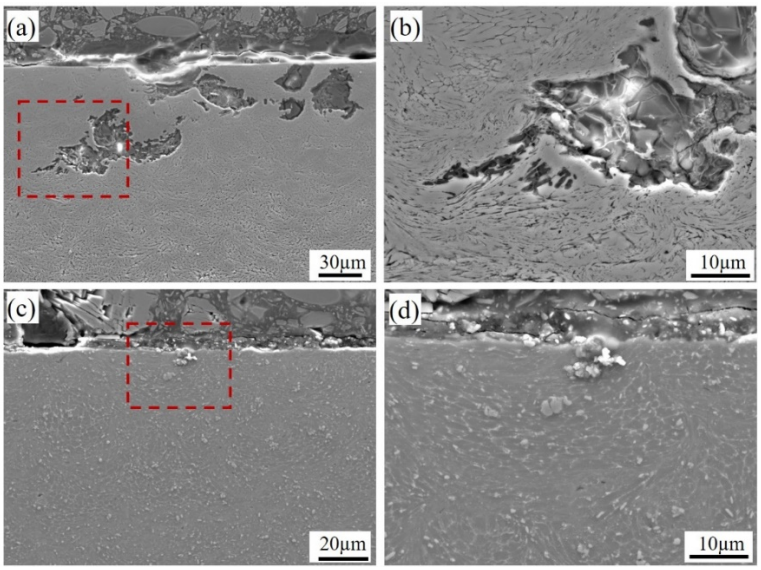

Fig. 8 SEM images showing the cross-sectional morphologies of the (a, b) 7075Al-C2 and (c, d) TiB_2/7075Al-C2 deposits after 7 days immersion in 0.6 M NaCl solution.

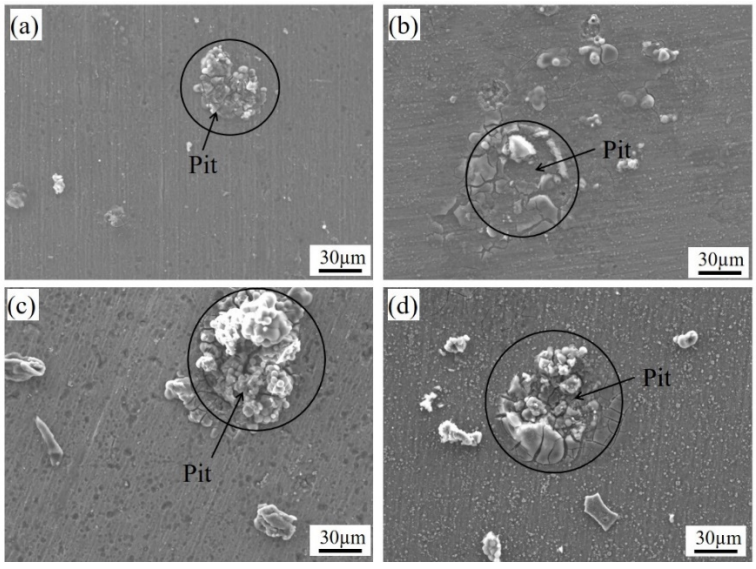

Fig. 9 The surface morphologies of the annealed samples after 7 day immersion in 0.6M NaCl solution: (a) 7075Al-C2-HT1; (b) TiB_2/7075Al-C2-HT1; (c) 7075Al-C2-HT2; (d) TiB_2/7075Al-C2-HT2.

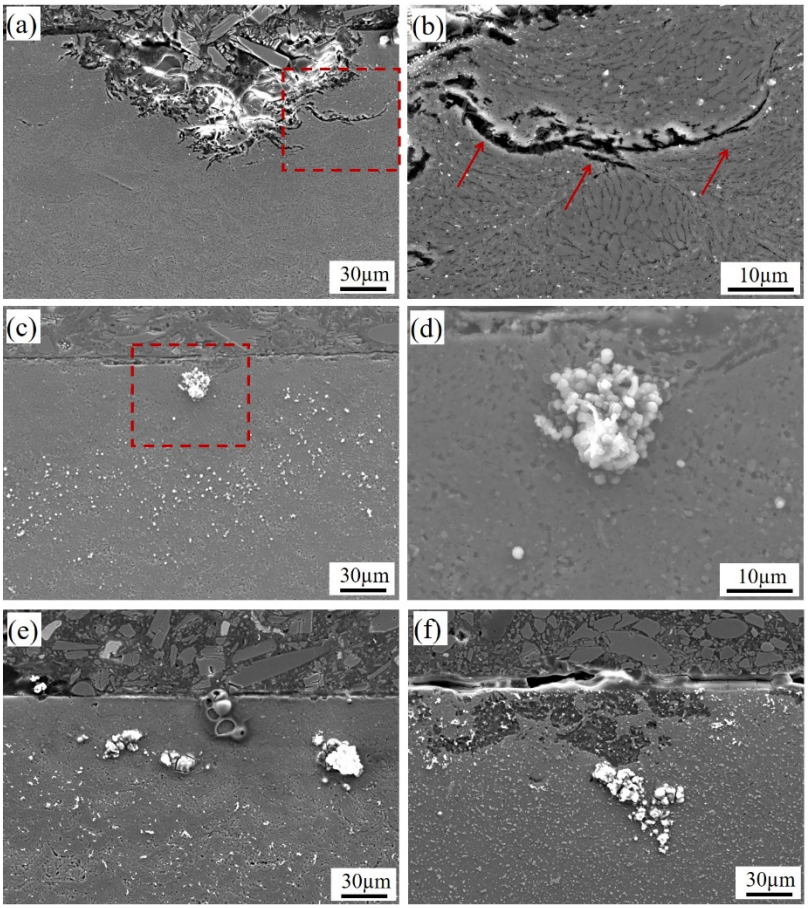

Fig. 10 SEM images showing the cross-sectional morphologies of the HT samples composite samples after 7 days immersion in 0.6 M NaCl solution: (a, b) 7075Al-C2-HT1; (c, d) TiB_2/7075Al-C2-HT1; (e) 7075Al-C2-HT2; (f) TiB_2/7075Al-C2-HT2. (b) and (d) show the corresponding magnified regions in (a) and (c), respectively.

Table 3 Summary of the average number ratio and average area fraction of the pits or caves in the eroded samples after 7 days immersion in 0.1 M and 0.6 M NaCl solutions.

Material	Average pits number ratio /cm^2		Average pits area fraction (%)	
	0.1 M	0.6 M	0.1 M	0.6 M
7075Al Bulk	12	26	0.13	0.40
7075Al-C1	11	35	2.1	6.7
TiB_2/7075Al-C1	1	3	0.12	0.60
7075Al-C2	13	24	3.6	14.2
TiB_2/7075Al-C2	2	4	0.40	0.90

7075Al-C2-HT1	–	16	–	8.0
TiB_2/7075Al-C2-HT1	–	6	–	2.3
7075Al-C2-HT2	–	3	–	0.80
TiB_2/7075Al-C2-HT2	–	7	–	3.6

3.2.2 Polarization studies

Fig. 11 shows the typical polarization curves for the bulk 7075Al alloy, CSed pure 7075Al, and TiB_2/7075Al composite coatings obtained in different conditions (C1 and C2). Values of corrosion potential (E_{corr}) and corrosion current densities (I_{corr}) obtained from the polarization curves are given in Table 4. E_{corr} represents the corrosion tendency of the material (a higher E_{corr} value indicating a lower tendency for corrosion) and I_{corr} directly reflects the corrosion rate of the material. Fig. 11a displays the results of the polarization curves of the samples tested in a 0.1 M NaCl solution. Clearly, bulk 7075Al possesses the highest E_{corr} (-0.74 V) and the lowest I_{corr} (2.25 E-6 A/cm^2) among all the tested samples, indicating that the bulk material has a better corrosion resistance than all coatings in a 0.1 M NaCl solution. For both CS processing conditions, average E_{corr} values of the composite coatings are higher than that of the pure 7075Al coatings, suggesting that the TiB_2/7075Al composite samples have lower corrosion tendencies from the view of corrosion thermodynamics. However, from the view of corrosion dynamics, I_{corr} of the composite coating is higher than that of the pure 7075Al coating, which indicates a higher corrosion rate for the composite coating. There is no significant difference in corrosion potential between C1 and C2 deposits tested in 0.1 M NaCl solution but the corrosion rates for C2 coatings appear to be slightly higher than those of the C1 coatings.

As previously for the 0.1 M NaCl solution, Fig. 11b demonstrates the results of polarization experiments in a 0.6 M NaCl solution. All the samples behave more active when the chloride concentration is increased. Again, the bulk material exhibits the lowest I_{corr} among all the tested samples but not the highest E_{corr} that belongs to the composite coating in both C1 and C2 conditions. Meanwhile, also for both conditions, the composite coating has the highest I_{corr} that is about ten times higher than that of the bulk material. Also, C2 samples exhibit systematically higher I_{corr} values than the C1 samples. Interestingly, evident current density plateau can be seen

from the catodic polartization curves in Fig. 11b when the samples were measured in a high Cl^- concentration.

From the above polarization analysis, one can conclude that corrosion resistance is decreasing in the order bulk material, C1 coatings, and then C2 coatings. Even though the TiB_2/7075Al composite coating seems to have a lower corrosion tendency from the thermodynamic point of view, it exhibits higher corrosion rates than the unreinforced 7075Al deposit.

Table 4 Results of potentiodynamic corrosion tests in 0.1 M and 0.6 M NaCl solutions.

Material	E_{corr} (V)		I_{corr} (E-5 A/cm^2)	
	0.1 M	0.6 M	0.1 M	0.6 M
7075Al Bulk	-0.74±0.02	-0.91±0.02	0.23±0.05	1.6±0.1
7075Al-C1	-0.88±0.02	-0.92±0.03	2.6±0.1	4.0±0.5
TiB_2/7075Al-C1	-0.81±0.02	-0.85±0.02	4.2±0.2	8.1±0.7
7075Al-C2	-0.88±0.02	-0.94±0.02	3.1±0.3	7.9±0.7
TiB_2/7075Al-C2	-0.83±0.02	-0.90±0.03	4.2±0.3	18±2
7075Al-C2-HT1	–	-0.88±0.02	–	1.1±0.2
TiB_2/7075Al-C2-HT1	–	-0.88±0.02	–	6.0±0.3
7075Al-C2-HT2	–	-0.90±0.02	–	29±3
TiB_2/7075Al-C2-HT2	–	-0.85±0.02	–	70±6

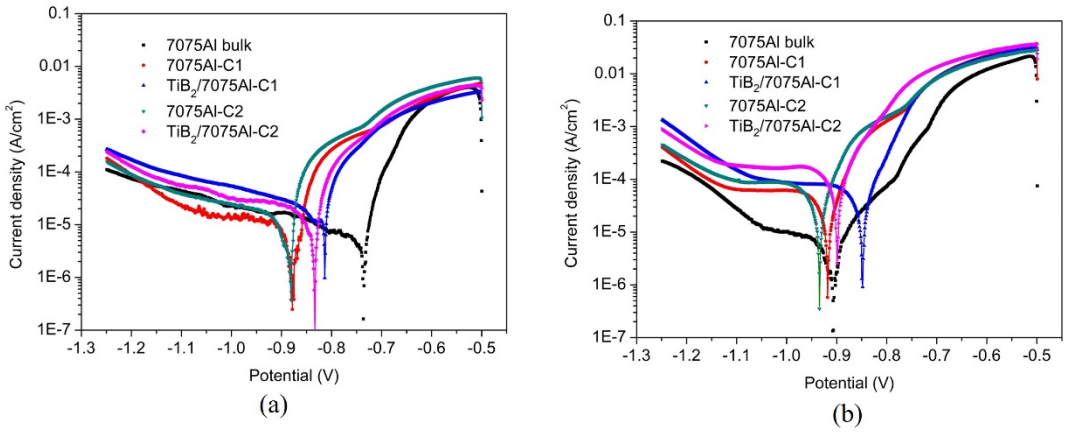

Fig. 11 Corrosion behavior of the bulk 7075Al, and sprayed coatings (a) in 0.1 M NaCl and (b)

in 0.6 M NaCl as determined by potentiodynamic polarization.

Further, electrochemical corrosion tests were performed on the HT1 and HT2 annealed coatings in 0.6 M NaCl solution. Corresponding polarization curves are given in Fig. 12 and E_{corr} and I_{corr} values deduced from the polarization curves are listed in Table 4. After an annealing treatment at 230 °C for 6 h, both pure 7075Al-C2 and TiB_2/7075Al-C2 composite coatings exhibit a significant decrease in I_{corr} and a slight increase in E_{corr} by comparison to the as-sprayed coatings. These results indicate an enhanced corrosion resistance of both coatings after low-temperature annealing treatment. On the contrary, when samples were annealed using HT2, i.e. at a higher temperature, I_{corr} of both coatings increased quite significantly, indicating that an annealing treatment can significantly influence the corrosion behavior of the CS coatings.

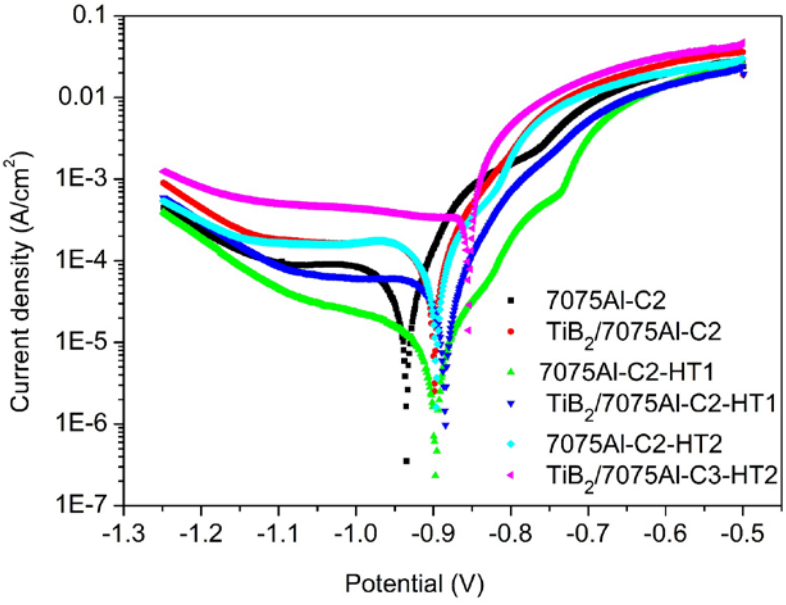

Fig. 12 Potentiodynamic polarization curves of the as-sprayed and annealed coatings.

3.2.3 Electrochemical impedance studies

EIS measurements were carried out in a 0.6 M NaCl solution at OCP to further explore the corrosion behavior of materials. Fig. 13 shows the experimental Nyquist plots for the bulk 7075Al and as-sprayed coatings which include two separate semicircles indicating two capacitance loops and two-time constants (Bode plots were given in the supplementary information). Amplitudes of the semicircles follow this order: bulk 7075Al-T6>7075Al-

C1>7075Al-C2>TiB_2/7075Al-C1> TiB_2/7075Al-C2. In Nyquist diagrams, the greater is the diameter of the capacitive loop, the lower is the corrosion rate of the sample [62]. From there, it is evident that the addition of TiB_2 particles decreases the corrosion resistance of the composite coating. Moreover, the C1 samples show again a better corrosion resistance than the C2 samples. EIS measurements are consistent with the polarization results.

EIS plots of the annealed C2 samples under different conditions are compared with those of the as-sprayed C2 samples, as illustrated in Fig. 13b. It is noted that the two-time constants are not clearly distinguished for the annealed samples, which have smaller diameters of the capacitive loop, especially for the HT2 samples.

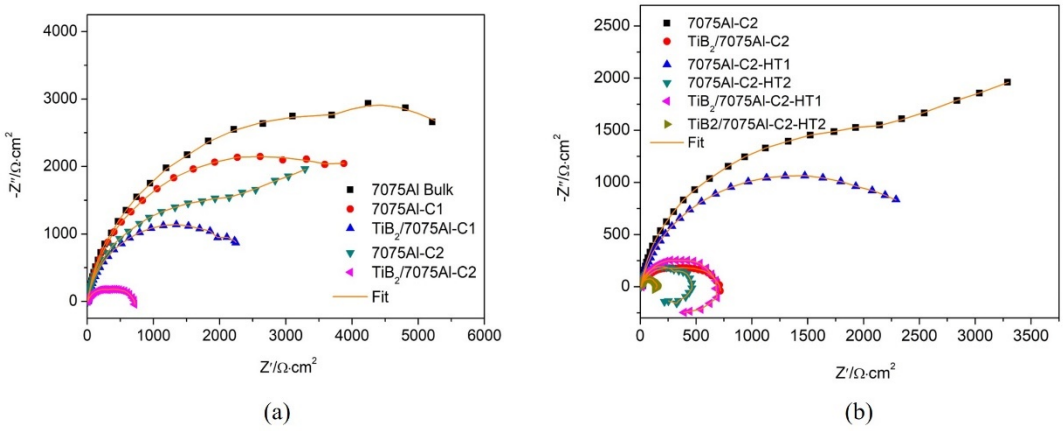

Fig. 13 Experimental and fitting of the Nyquist plots of the (a) as-sprayed and (b) annealed samples.

From the typical EIS plots, two different electrical equivalent circuits (EEC) were proposed to fit the experimental results of the as-sprayed and annealed coatings, as described in Fig. 14a and b, respectively. In the case of the as-sprayed coatings, an EEC with two-time constants was fitted well with the experimental data as previously suggested [23, 42] for the CSed Al alloy coatings; In this EEC, R_s represents the solution resistance and is independent of time; R_{ct} is the charge transfer resistance and the capacitor C is replaced by a constant phase element (CPE), which composed of two components: CPE-Y_0 and n. Y_0 is the frequency-independent, and n is a dimensionless index [62]. CPE_{dl} corresponds to the capacitance of the double layer of the coating/electrolyte interface at medium frequency range; R_{film} is related to

the oxide film dissolution/diffusion through an oxide film at the inter-splat boundaries and the CPE_{film} corresponds to the capacitance of the oxide film at low-frequency range. The fitting results are given in Table 5. The quality of fitting was evaluated by the chi-squared (χ^2) error value. R_{ct} is an important parameter that is directly dependent on the active protection provided by the surface layer. It is evident that the R_{ct} of bulk 7075Al is much higher than that of coatings. When compared to the pure 7075Al coating, a slight decrease of R_{ct} is observed for the TiB_2/7075Al composite coating. In addition, the C1 samples possess higher R_{ct} values than the C2 samples. A similar tendency is observed for $R_{film.}$ According to previous studies [62, 63], the sum of R_{ct} and R_{film} can be used to characterize corrosion resistance. It appears that way that the corrosion resistance follows the order: bulk 7075Al>7075Al-C1>7075Al-C2>TiB_2/7075Al-C1> TiB_2/7075Al-C2, which again is consistent with the polarization curves results.

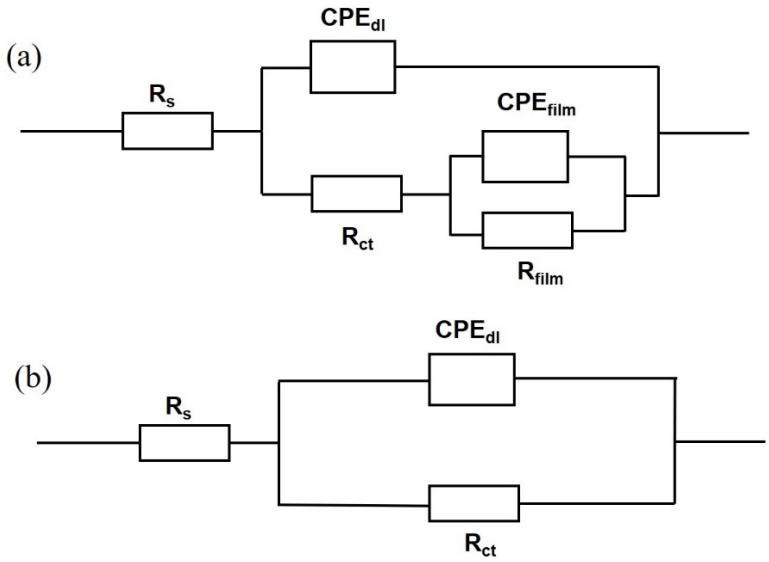

Fig. 14 Electrical equivalent circuits used to fit the EIS data: (a) bulk 7075Al and as-sprayed coatings; (b) annealed samples.

In the case of annealed samples, the contribution of R_{film}/CPE_{film} constant is weakened or even disappeared due to the elimination of inter-splat boundaries. Thus, an EEC with one-time constant was applied to fit the obtained impedance data (Fig. 14b). It can be noted that the HT1 samples exhibit higher R_{ct} values as compared to the as-sprayed samples, while the HT2 composite sample possesses the lowest R_{ct} value. Nevertheless, lower sum values (R_{ct} + R_{film})

of the HT2 annealed samples suggest lower uniform corrosion resistance compared to the as-sprayed sate.

Table 5 Fitted EIS parameters for the bulk and as-sprayed coatings.

Sample	R_s (Ω cm^2)	CPE_{dl}-Y_o (S s^n cm^{-2})	n_{dl}	R_{ct} (kΩ cm^2)	CPE_{film}-Y_o (S s^n cm^{-2})	n_{film}	R_{film} (kΩ cm^2)	χ^2	R_{ct}+R_{film} (kΩ cm^2)
Bulk 7075Al	12.85	6.60×10^{-6}	0.93	1.41	4.56×10^{-6}	0.54	4.33	4.3×10^{-4}	5.74
7075Al-C1	9.12	6.54×10^{-6}	0.91	0.53	4.28×10^{-6}	0.82	3.82	1.7×10^{-3}	4.35
TiB_2/7075Al-C1	8.70	7.98×10^{-6}	0.91	0.40	5.26×10^{-6}	0.87	1.99	2.6×10^{-3}	2.39
7075Al-C2	10.18	6.19×10^{-6}	0.93	0.18	1.87×10^{-5}	0.94	2.26	3.0×10^{-4}	2.44
TiB_2/7075Al-C2	9.31	7.37×10^{-6}	0.82	0.15	1.98×10^{-5}	0.66	0.41	7.5×10^{-3}	0.61
7075Al-C2-HT1	5.60	1.72×10^{-4}	–	2.21	–	–	–	1.1×10^{-3}	2.21
7075Al-C2-HT2	8.16	4.27×10^{-4}	–	0.45	–	–	–	2.9×10^{-4}	0.45
TiB_2/7075Al-C2-HT1	8.82	1.03×10^{-5}	–	0.26	–	–	–	1.2×10^{-5}	0.26
TiB_2/7075Al-C2-HT2	10.92	5.08×10^{-5}	–	0.09	–	–	–	1.1×10^{-5}	0.09

4. Discussions

In this study, the influence of processing parameters and subsequent annealing treatments on the corrosion behavior of the CSed pure 7075Al and TiB_2/7075Al composite coatings in saltwater was investigated using Tafel polarization, EIS, and immersion tests. From experimental analysis, the following three general statements can be drawn: i) both coatings, whatever the conditions, show reduced corrosion resistance compared with the bulk 7075Al alloy; ii) the TiB_2/7075Al composite coatings show a lower corrosion tendency but an increased dynamic corrosion rate compared to the pure 7075Al coatings; iii) a low-annealing temperature treatment (230 °C/6h) is beneficial for the corrosion resistance of as-sprayed coatings, however, a higher annealing temperature (412 °C/4h) results in a significant decrease in their corrosion

resistance. Combining with microstructural evolutions, the corrosion mechanisms of the as-sprayed and annealed composite coatings are discussed, which may help further improve and optimize the corrosion resistance.

From a general point of view, the specific microstructure of a sample is a decisive factor in its corrosion resistance [64]. As reported by previous studies [19, 65], bulk 7075 sample issued from a hot-rolling process exhibits a homogenous structure with micron-sized grains, which is beneficial for the corrosion resistance of the material in saltwater. As for the as-sprayed pure 7075Al and TiB_2/7075Al composite coatings, they are formed through plastic deformation and bonding of the particles, thus encompassing inter-particle boundaries and micro-pores. Previous studies revealed that both the porosity and the degree of plastic deformation of the particles also play important roles in determining the corrosion behavior of CSed Al alloy coatings [19, 22]. On the one hand, according to Ngai *et al.* [19], limited particle deformation and a high degree of resultant porosity yield a high corrosion rate due to the formation of severe micro-crevice corrosion and irregular pitting network on the corroded surface. Therefore, a porous structure can significantly lower the corrosion resistance of the coating. On the other hand, according to the studies of Balani *et al.* [22] and Meydanoglu *et al.* [18], the presence of active sites as a result of a high degree of deformation may also lead to high corrosion current densities.

In the present study, both the air-processed and He-processed coatings show a relatively dense structure with only some small micro-pores at the junctions of the splats. Therefore, the degree of plastic deformation dominates a key role in affecting the corrosion performance of the CSed coatings. Using He as the propellant gas (C2 condition) effectively accelerates particles to a much higher impact velocity and thus greater particle deformation occurs when compared to air-processed coatings (see Fig. 2 and Fig. 3). It may thus be inferred that the greater deformation generated in the C2 coatings promotes a number of active sites for corrosion, resulting in a higher corrosion rate than the C1 coatings. It was reported that the dislocations generated by severe plastic deformation of the particles upon impact contribute to the increment in the number of precipitates [66, 67]. According to the TEM results (see Fig. 4), a high density of fine precipitates, is distributed homogeneously within the matrix of C2

deposits. Compared to the Al matrix, these precipitates have higher potential, acting as anode and promoting the corrosion process in saltwater [68-70]. Consequently, precipitates at the GBs degrade the corrosion resistance of the CSed samples [71]. Therefore, the degree of plastic deformation affects significantly the microstructure, formation of precipitates, and thereby the corrosion behavior of CSed coatings.

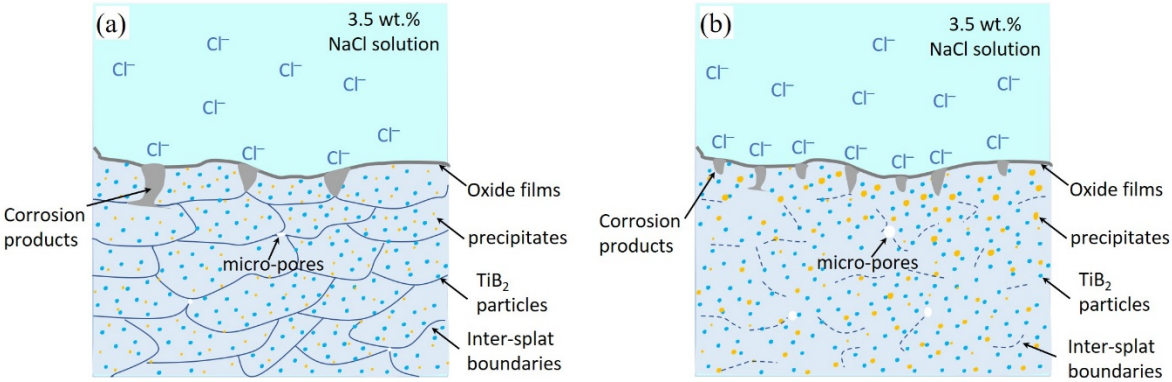

Fig. 15 Schematic diagram of corrosion process mechanisms of (a) as-sprayed and (b) HT2 annealed TiB_2/7075Al composite coatings.

Based on above analysis, the corrosion process mechanisms can be further summarized. As illustrated by the schematic diagram in Fig. 15a, Cl^- in the NaCl solution immerges in the coating surface, destroys the oxide film, and results in the anodic dissolution ($Al \rightarrow Al^{3+} + 3e^-$) and production of Al^{3+} [72, 73]. Accordingly, the thin oxide films formed on the coating surface before immersion usually act as the cathode. The cathodic reactions may include ($O_2 + 2H_2O + 4e^- \rightarrow 4OH^-$) and ($2H_2O + 2e^- \rightarrow 2OH^- + H_2\uparrow$) [34]. As shown in Fig. 11b, the presence of current density plateau indicates a diffusion control process, which likely results from low oxygen concentration and the slow diffusion of oxygen to the cathode areas [64]. In this study, although Ar was purged for 15 min before polarization measurements, the oxygen dissolved within the NaCl solution cannot be completely removed. Therefore, as the polarization current density increases, the concentration polarization caused by oxygen diffusion control is strengthened, forming a plateau-like polarization curve. Actually, the current density plateau observed in the samples measured in a 0.6M NaCl is much more remarkable compared to those tested in a 0.1 M NaCl solution (Fig. 11a). This probably because a high Cl^- concentration could result in a faster cathodic polarization reaction, and thereby faster oxygen consumption, causing

the concentration polarization and appearance of such a plateau. When the cathode potential decreases to a more negative level, the water reduction reaction may occur in the NaCl solution, and the cathode process will be composed of oxygen reduction ($O_2 + 2H_2O + 4e^- \rightarrow 4OH^-$) and water reduction ($2H_2O + 2e^- \rightarrow 2OH^- + H_2\uparrow$). Then, the metallic cations (Al^{3+}) react with hydroxyl ions (OH^-) to form the corrosion products ($Al(OH)_3$). The amount of corrosion products increases with Cl^- concentration and the duration of immersion time. Moreover, the defects (e.g. micro-pores and poorly bonded inter-splat boundaries) promote the entrance of corrosive solution inside the coating, and the crevices initiate and propagate along with the interparticle interfaces. As a result, the entire particle would be peeled off, forming a large cave (Fig. 8a and b). Therefore, the corroded surface morphologies of as-sprayed samples after corrosion tests reveal a pitting corrosion mechanism, and the corrosion resistance of the coatings is thus largely reduced when compared to the bulk material.

Considering that both the particle plastic deformation degree and the inter-splat boundary can influence the corrosion resistance of as-sprayed coatings, annealing treatments should play a role in reducing corrosion susceptibility of the coatings. Indeed, after a low-temperature annealing treatment (230 ℃/6h), our samples displayed an enhanced corrosion resistance. This is probably because of stress relief and dislocations elimination, reducing the number of active sites for corrosion. The XRD patterns of 7075Al powder, 7075Al-C2 coating, and 7075Al-C2-HT1 and 7075Al-C2-HT2 coatings are shown in Supplementary Fig.2. Supplementary Fig.2b shows that the Al (111) peak of the as-sprayed coating widens and shifts to a higher angle with respect to that of the initial powder, which suggests the formation of defects like lattice strain and dislocations during the CS process. With increasing the annealing temperature from 230 °C to 412 °C, the peak gradually moves back to lower angles. Besides, a reduction in peak width can be also observed after annealing treatment. The reduction in peak width and the peak shifting in XRD patterns may result from the elimination of defects like lattice strain and dislocations within the as-sprayed coating after annealing treatment. However, after a higher temperature annealing treatment (412℃/4h), corrosion resistance was noticeably degraded. As shown in Fig. 15b, even though less inter-splat boundaries are present within the HT2 treated coatings, the presence of more evident pores resulting from interfaces migration and micro-

pores growth can promote the corrosion process. More importantly, the remarkable grain growth and more prominent precipitates proved to be detrimental for the corrosion resistance [74]. Therefore, when considering the use of heat-treating for improving the corrosion resistance of the CSd coatings, all of the aspects of microstructural changes, such as defects, precipitation, and grain size, have to be taken into account.

Experimental results also show that the addition of nano-TiB_2 reinforcement has a significant influence on the corrosion behavior of the pure 7075Al coatings. On the one hand, static immersion tests indicated that the addition of nano-TiB_2 particles in the 7075Al matrix leads to stable oxide films with only very few pits on the corroded surface. Thus, during immersion in a NaCl solution, a protective oxide layer is formed on the surface of the samples, probably composed of both Al and Ti oxides [75]. The presence of this oxide layer can protect the underlying layer from further corrosion attack. Meanwhile, relatively higher E_{corr} values of the composite coatings also indicate lower corrosion tendency from the point of view of corrosion thermodynamics compared with the pure 7075Al coatings. On the other hand, higher I_{corr} values and much lower R_{ct} values of the composite coating display higher corrosion rates compared to pure 7075Al coating. It was suggested that TiB_2 is semi-conductive with an electrical resistivity of approximately 15×10^{-6} ohm·cm [76, 77]. Hence, this corrosion behavior of the composite's coatings could be due to a galvanic coupling between a noble reinforcement (TiB_2) and the more active Al matrix [77]. The potential difference between Al matrix and TiB_2 (about 252 mV) is large enough to induce micro-galvanic corrosion [76]. The galvanic coupling between TiB_2 particles and the Al matrix provides a cathode site for hydrogen evolution. As a result, corrosion progress mainly occurs at GB having a mass of TiB_2 particles and propagates into the composite. Localized dissolution at the matrix/TiB_2 interface creating a localized acidic environment can further increase the Al matrix dissolution to form blisters. In favorable conditions, these blisters extend and break to produce a new open pit. Similar corrosion behavior was reported in TiB_2/Al, TiB_2/Al-4%Cu, and TiB_2/AlSi composite systems produced from stir casting [76, 77]. Therefore, despite the relatively low porosity level, the galvanic coupling effect induced by the presence of TiB_2 particles significantly degrades the finial corrosion performance of the composite sample.

5. Conclusions

Corrosion behavior of the CSed 7075Al based composite coatings was investigated using Tafel polarization, EIS, and immersion tests in 0.1 M and 0.6 M NaCl solutions. Electrochemical tests revealed that the TiB_2/7075Al composite coatings exhibit higher corrosion rates resulting from a galvanic coupling between the noble TiB_2 reinforcement particles and the more active Al matrix when compared to pure 7075Al coatings. Moreover, greater plastic deformation in He-processed samples results also in reduced corrosion resistance when compared to air-processed samples due to the larger generation of precipitates and defects like dislocations within the samples. Effects of annealing treatments on the corrosion behavior of these coatings were considered and it was found that corrosion performance of the as-sprayed coatings could be improved at the low annealing temperature (230 °C/6h) while an increase of the annealing temperature up to 412 ℃ for 4 h resulted in a further decrease in the corrosion resistance for both deposits. This phenomenon can be explained by the beneficial effect of lattice strain and dislocations annihilation at relatively low annealing temperature (230 °C/6h) while evident grain and precipitates growth occurs at a high temperature (412 °C/4h).

Acknowledgments

Xinliang XIE is grateful for the financial support of the China Scholarship Council for his Ph.D. project. The support of the Conseil Regional du Nord-Pas de Calais and the European Regional Development Fund (ERDF) for the microscopy facility in Lille, France is also gratefully acknowledged.

References

[1] Santosh Kumar, Manoj Kumar, Neeru Jindal, Overview of cold spray coatings applications and comparisons: a critical review, World Journal of Engineering, (2020), Vol. 17 No. 1, pp. 27-51.

[2] SEYYED MOSTAFA Hassani-Gangaraj, ATIEH Moridi, MARIO Guagliano, Critical review of corrosion protection by cold spray coatings, Surface Engineering, 31 (2015), 803-815.

[3] Fernando Santos da Silva, Núria Cinca, Sergi Dosta, Irene Garcia Cano, Josep Maria Guilemany, Assis Vicente Benedetti, Cold gas spray coatings: basic principles, corrosion

protection and applications, Eclética Química Journal, 42 (2017), 09-32.

[4] Wenya Li, Hamid Assadi, Frank Gaertner, Shuo Yin, A review of advanced composite and nanostructured coatings by solid-state cold spraying process, Critical Reviews in Solid State and Materials Sciences, 44 (2019), 109-156.

[5] W-Y Li, C Zhang, H-T Wang, XP Guo, HL Liao, C-J Li, C Coddet, Significant influences of metal reactivity and oxide films at particle surfaces on coating microstructure in cold spraying, Appl. Surf. Sci., 253 (2007), 3557-3562.

[6] Tobias Schmidt, Frank Gärtner, Hamid Assadi, Heinrich Kreye, Development of a generalized parameter window for cold spray deposition, Acta Mater., 54 (2006), 729-742.

[7] RC Dykhuizen, MF Smith, Gas dynamic principles of cold spray, J. Therm. Spray Technol., 7 (1998), 205-212.

[8] MR Rokni, SR Nutt, CA Widener, VK Champagne, RH Hrabe, Review of relationship between particle deformation, coating microstructure, and properties in high-pressure cold spray, J. Therm. Spray Technol., 26 (2017), 1308-1355.

[9] Rija Nirina Raoelison, Yingchun Xie, Thaneshan Sapanathan, Marie Pierre Planche, Robin Kromer, Sophie Costil, Cécile Langlade, Cold gas dynamic spray technology: a comprehensive review of processing conditions for various technological developments till to date, Addit. Manuf., 19 (2018), 134-159.

[10] S Dosta, M Couto, JM Guilemany, Cold spray deposition of a WC-25Co cermet onto Al7075-T6 and carbon steel substrates, Acta Mater., 61 (2013), 643-652.

[11] Eric Irissou, Jean-Gabriel Legoux, Bernard Arsenault, Christian Moreau, Investigation of Al-Al2O3 cold spray coating formation and properties, J. Therm. Spray Technol., 16 (2007), 661-668.

[12] Wen-Ya Li, Chao Zhang, Xueping Guo, Chang-Jiu Li, Hanlin Liao, C Coddet, Study on impact fusion at particle interfaces and its effect on coating microstructure in cold spraying, Appl. Surf. Sci., 254 (2007), 517-526.

[13] Xinliang Xie, Chaoyue Chen, Gang Ji, Run Xu, Zhanqiu Tan, Yingchun Xie, Zhiqiang Li, Hanlin Liao, A novel approach for fabricating a CNT/AlSi composite with the self-aligned nacre-like architecture by cold spraying, Nano Materials Science, 1 (2019), 137-141.

[14] Tanvir Hussain, DG McCartney, PH Shipway, T Marrocco, Corrosion behavior of cold

sprayed titanium coatings and free standing deposits, J. Therm. Spray Technol., 20 (2011), 260-274.

[15] Heli Koivuluoto, Giovanni Bolelli, Luca Lusvarghi, Fabrizio Casadei, Petri Vuoristo, Corrosion resistance of cold-sprayed Ta coatings in very aggressive conditions, Surf. Coat. Technol., 205 (2010), 1103-1107.

[16] Ying-Kang Wei, Yu-Juan Li, Yue Zhang, Xiao-Tao Luo, Chang-Jiu Li, Corrosion resistant nickel coating with strong adhesion on AZ31B magnesium alloy prepared by an in-situ shot-peening-assisted cold spray, Corros. Sci., 138 (2018), 105-115.

[17] SJ Choi, HS Lee, JW Jang, S Yi, Corrosion behavior in a 3.5 wt% NaCl solution of amorphous coatings prepared through plasma-spray and cold-spray coating processes, Metals and Materials International, 20 (2014), 1053-1057.

[18] Onur Meydanoglu, Bertrand Jodoin, E Sabri Kayali, Microstructure, mechanical properties and corrosion performance of 7075 Al matrix ceramic particle reinforced composite coatings produced by the cold gas dynamic spraying process, Surf. Coat. Technol., 235 (2013), 108-116.

[19] Sieglind Ngai, Tungwai Ngai, Florian Vogel, William Story, Gregory B Thompson, Luke N Brewer, Saltwater corrosion behavior of cold sprayed AA7075 aluminum alloy coatings, Corros. Sci., 130 (2018), 231-240.

[20] W-Y Li, Ga Zhang, HL Liao, Christian Coddet, Characterizations of cold sprayed TiN particle reinforced Al2319 composite coating, J. Mater. Process. Technol., 202 (2008), 508-513.

[21] W-Y Li, G Zhang, C Zhang, O Elkedim, H Liao, C Coddet, Effect of ball milling of feedstock powder on microstructure and properties of TiN particle-reinforced Al alloy-based composites fabricated by cold spraying, J. Therm. Spray Technol., 17 (2008), 316-322.

[22] Kantesh Balani, T Laha, Arvind Agarwal, J Karthikeyan, N Munroe, Effect of carrier gases on microstructural and electrochemical behavior of cold-sprayed 1100 aluminum coating, Surf. Coat. Technol., 195 (2005), 272-279.

[23] FS Da Silva, J Bedoya, S Dosta, N Cinca, IG Cano, JM Guilemany, AV Benedetti, Corrosion characteristics of cold gas spray coatings of reinforced aluminum deposited onto carbon steel, Corros. Sci., 114 (2017), 57-71.

[24] Brian S DeForce, Timothy J Eden, John K Potter, Cold spray Al-5% Mg coatings for the corrosion protection of magnesium alloys, J. Therm. Spray Technol., 20 (2011), 1352-1358.

[25] Yongshan Tao, Tianying Xiong, Chao Sun, Lingyan Kong, Xinyu Cui, Tiefan Li, Guang-Ling Song, Microstructure and corrosion performance of a cold sprayed aluminium coating on AZ91D magnesium alloy, Corros. Sci., 52 (2010), 3191-3197.

[26] Mohammad Diab, Xin Pang, Hamid Jahed, The effect of pure aluminum cold spray coating on corrosion and corrosion fatigue of magnesium (3% Al-1% Zn) extrusion, Surf. Coat. Technol., 309 (2017), 423-435.

[27] Chunchun Ma, Xiaofang Liu, Chungen Zhou, Cold-sprayed Al coating for corrosion protection of sintered NdFeB, J. Therm. Spray Technol., 23 (2014), 456-462.

[28] Chunjie Huang, Wenya Li, Zhihan Zhang, Maosen Fu, Marie-pierre Planche, Hanlin Liao, Ghislain Montavon, Modification of a cold sprayed SiCp/Al5056 composite coating by friction stir processing, Surf. Coat. Technol., 296 (2016), 69-75.

[29] HR Lashgari, AR Sufizadeh, M Emamy, The effect of strontium on the microstructure and wear properties of A356–10% B4C cast composites, Mater. Des., 31 (2010), 2187-2195.

[30] Liu Zhang, Hanqing Xu, Zhi Wang, Qinggang Li, Junyan Wu, Mechanical properties and corrosion behavior of Al/SiC composites, J. Alloys Compd., 678 (2016), 23-30.

[31] Michael Oluwatosin Bodunrin, Kenneth Kanayo Alaneme, Lesley Heath Chown, Aluminium matrix hybrid composites: a review of reinforcement philosophies; mechanical, corrosion and tribological characteristics, Journal of materials research and technology, 4 (2015), 434-445.

[32] Qiang Wang, Qi Sun, Ming-Xing Zhang, Wen-Juan Niu, Chang-Bin Tang, Kuai-She Wang, Xing Rui, Le Zhai, Lu Wang, The influence of cold and detonation thermal spraying processes on the microstructure and properties of Al-based composite coatings on Mg alloy, Surf. Coat. Technol., 352 (2018), 627-633.

[33] Qiang Wang, Kevin Spencer, Nick Birbilis, Ming-Xing Zhang, The influence of ceramic particles on bond strength of cold spray composite coatings on AZ91 alloy substrate, Surf. Coat. Technol., 205 (2010), 50-56.

[34] Ying-Kang Wei, Xiao-Tao Luo, Yi Ge, Xin Chu, Guo-Sheng Huang, Chang-Jiu Li, Deposition of fully dense Al-based coatings via in-situ micro-forging assisted cold spray for excellent corrosion protection of AZ31B magnesium alloy, J. Alloys Compd., 806 (2019), 1116-1126.

[35] Yongshan Tao, Tianying Xiong, Chao Sun, Huazi Jin, Hao Du, Tiefan Li, Effect of α-Al2O3 on the properties of cold sprayed Al/α-Al2O3 composite coatings on AZ91D magnesium alloy, Appl. Surf. Sci., 256 (2009), 261-266.

[36] K Spencer, DM Fabijanic, M-X Zhang, The use of Al–Al2O3 cold spray coatings to improve the surface properties of magnesium alloys, Surf. Coat. Technol., 204 (2009), 336-344.

[37] Yingying Wang, Bernard Normand, Nicolas Mary, Min Yu, Hanlin Liao, Effects of ceramic particle size on microstructure and the corrosion behavior of cold sprayed SiCp/Al 5056 composite coatings, Surf. Coat. Technol., 315 (2017), 314-325.

[38] Hengyong Bu, Mohammed Yandouzi, Chen Lu, Daniel MacDonald, Bertrand Jodoin, Cold spray blended Al+ Mg17Al12 coating for corrosion protection of AZ91D magnesium alloy, Surf. Coat. Technol., 207 (2012), 155-162.

[39] A Lekatou, AE Karantzalis, A Evangelou, V Gousia, Gy Kaptay, Z Gácsi, P Baumli, A Simon, Aluminium reinforced by WC and TiC nanoparticles (ex-situ) and aluminide particles (in-situ): Microstructure, wear and corrosion behaviour, Materials & Design (1980-2015), 65 (2015), 1121-1135.

[40] Seyed Omid Reza Sheykholeslami, Reza Taherzadeh Mousavian, Dermot Brabazon, Corrosion behaviour of rolled A356 matrix composite reinforced with ceramic particles, International Journal of Materials Research, 107 (2016), 1100-1111.

[41] Xiawei Yang, Wenya Li, Siqi Yu, Yaxin Xu, Kaiwei Hu, Yaobang Zhao, Electrochemical characterization and microstructure of cold sprayed AA5083/Al2O3 composite coatings, J. Mater. Sci. Technol., (2020),

[42] Kang Yang, Wenya Li, Yaxin Xu, Xiawei Yang, Using friction stir processing to augment corrosion resistance of cold sprayed AA2024/Al2O3 composite coatings, J. Alloys Compd., 774 (2019), 1223-1232.

[43] Xinliang Xie, Yu Ma, Chaoyue Chen, Gang Ji, Christophe Verdy, Hongjian Wu, Zhe Chen, Sheng Yuan, Bernard Normand, Shuo Yin, Cold spray additive manufacturing of metal matrix composites (MMCs) using a novel nano-TiB2-reinforced 7075Al powder, J. Alloys Compd., (2019), 152962.

[44] Yingying Wang, Bernard Normand, Nicolas Mary, Min Yu, Hanlin Liao, Microstructure and corrosion behavior of cold sprayed SiCp/Al 5056 composite coatings, Surf. Coat. Technol.,

251 (2014), 264-275.

[45] Zhichao Zhang, Fuchun Liu, En-Hou Han, Long Xu, Paul C Uzoma, Effects of Al2O3 on the microstructures and corrosion behavior of low-pressure cold gas sprayed Al 2024-Al2O3 composite coatings on AA 2024-T3 substrate, Surf. Coat. Technol., 370 (2019), 53-68.

[46] Mengxing Chen, Xiaopeng Li, Gang Ji, Yi Wu, Zhe Chen, Wouter Baekelant, Kim Vanmeensel, Haowei Wang, Jean-Pierre Kruth, Novel composite powders with uniform TiB2 nano-particle distribution for 3D printing, Applied Sciences, 7 (2017), 250.

[47] Pierre Coddet, Christophe Verdy, Christian Coddet, François Debray, Effect of cold work, second phase precipitation and heat treatments on the mechanical properties of copper–silver alloys manufactured by cold spray, Mater. Sci. Eng., A, 637 (2015), 40-47.

[48] M Arshad Choudhry, Muhammad Ashraf, Effect of heat treatment and stress relaxation in 7075 aluminum alloy, J. Alloys Compd., 437 (2007), 113-116.

[49] Michael Bauccio, ASM metals reference book, ASM international, 1993.

[50] Edson Costa Santos, Masanari Shiomi, Kozo Osakada, Tahar Laoui, Rapid manufacturing of metal components by laser forming, International Journal of Machine Tools and Manufacture, 46 (2006), 1459-1468.

[51] MR Rokni, CA Widener, GA Crawford, Microstructural evolution of 7075 Al gas atomized powder and high-pressure cold sprayed deposition, Surf. Coat. Technol., 251 (2014), 254-263.

[52] Xiao Peng Li, Gang Ji, Z Chen, Ahmed Addad, Y Wu, HW Wang, Jef Vleugels, Jan Van Humbeeck, Jean-Pierre Kruth, Selective laser melting of nano-TiB2 decorated AlSi10Mg alloy with high fracture strength and ductility, Acta Mater., 129 (2017), 183-193.

[53] Xiao-Tao Luo, Ying-Kang Wei, Yan Wang, Chang-Jiu Li, Microstructure and mechanical property of Ti and Ti6Al4V prepared by an in-situ shot peening assisted cold spraying, Mater. Des., 85 (2015), 527-533.

[54] Xinliang Xie, Chaoyue Chen, Yingchun Xie, Zhongming Ren, Eric Aubry, Gang Ji, Hanlin Liao, A novel approach for fabricating Ni-coated FeSiAl soft magnetic composite via cold spraying, J. Alloys Compd., 749 (2018), 523-533.

[55] Shuo Yin, Pasquale Cavaliere, Barry Aldwell, Richard Jenkins, Hanlin Liao, Wenya Li, Rocco Lupoi, Cold spray additive manufacturing and repair: Fundamentals and applications, Addit. Manuf., 21 (2018), 628-650.

[56] Mica Grujicic, CL Zhao, Chenning Tong, WS DeRosset, D Helfritch, Analysis of the impact velocity of powder particles in the cold-gas dynamic-spray process, Mater. Sci. Eng., A, 368 (2004), 222-230.

[57] Yu Zou, Wen Qin, Eric Irissou, Jean-Gabriel Legoux, Stephen Yue, Jerzy A Szpunar, Dynamic recrystallization in the particle/particle interfacial region of cold-sprayed nickel coating: Electron backscatter diffraction characterization, Scripta Mater., 61 (2009), 899-902.

[58] Kicheol Kang, Juyeon Won, Gyuyeol Bae, Sangmin Ha, Changhee Lee, Interfacial bonding and microstructural evolution of Al in kinetic spraying, J. Mater. Sci., 47 (2012), 4649-4659.

[59] MR Rokni, CA Widener, VK Champagne, GA Crawford, SR Nutt, The effects of heat treatment on 7075 Al cold spray deposits, Surf. Coat. Technol., 310 (2017), 278-285.

[60] T Marlaud, A Deschamps, F Bley, W Lefebvre, B Baroux, Influence of alloy composition and heat treatment on precipitate composition in Al–Zn–Mg–Cu alloys, Acta Mater., 58 (2010), 248-260.

[61] JJ Pang, FC Liu, J Liu, MJ Tan, DJ Blackwood, Friction stir processing of aluminium alloy AA7075: microstructure, surface chemistry and corrosion resistance, Corros. Sci., 106 (2016), 217-228.

[62] Mark E Orazem, Bernard Tribollet, Electrochemical impedance spectroscopy, New Jersey, (2008), 383-389.

[63] J Ross Macdonald, E Barsoukov, Impedance spectroscopy: theory, experiment, and applications, History, 1 (2005), 1-13.

[64] Philippe Marcus, Corrosion mechanisms in theory and practice, Marcel Dekker, Inc., New York (2002).

[65] Alexandre Goloborodko, Tsutomu Ito, Xiaoyong Yun, Yoshinobu Motohashi, Goroh Itoh, Friction stir welding of a commercial 7075-T6 aluminum alloy: grain refinement, thermal stability and tensile properties, Mater. Trans., 45 (2004), 2503-2508.

[66] D Wang, DR Ni, ZY Ma, Effect of pre-strain and two-step aging on microstructure and stress corrosion cracking of 7050 alloy, Mater. Sci. Eng., A, 494 (2008), 360-366.

[67] Kaka Ma, Tao Hu, Hanry Yang, Troy Topping, Ali Yousefiani, Enrique J Lavernia, Julie M Schoenung, Coupling of dislocations and precipitates: impact on the mechanical behavior of

ultrafine grained Al–Zn–Mg alloys, Acta Mater., 103 (2016), 153-164.

[68] Jinghui Li, Fuguo Li, Xinkai Ma, Jiang Li, Shan Liang, Effect of grain boundary characteristic on intergranular corrosion and mechanical properties of severely sheared Al-Zn-Mg-Cu alloy, Mater. Sci. Eng., A, 732 (2018), 53-62.

[69] HC Fang, FH Luo, KH Chen, Effect of intermetallic phases and recrystallization on the corrosion and fracture behavior of an Al-Zn-Mg-Cu-Zr-Yb-Cr alloy, Mater. Sci. Eng., A, 684 (2017), 480-490.

[70] Joachim Wloka, Theo Hack, Sannakaisa Virtanen, Influence of temper and surface condition on the exfoliation behaviour of high strength Al–Zn–Mg–Cu alloys, Corros. Sci., 49 (2007), 1437-1449.

[71] Hao Wang, Chengyi Ning, Yihui Huang, Zhenya Cao, Xiaoxiao Chen, Wenwu Zhang, Improvement of abrasion resistance in artificial seawater and corrosion resistance in NaCl solution of 7075 aluminum alloy processed by laser shock peening, Optics and Lasers in Engineering, 90 (2017), 179-185.

[72] R Winston Revie, Corrosion and corrosion control: an introduction to corrosion science and engineering, John Wiley & Sons, 2008, 280.

[73] WA Badawy, FM Al-Kharafi, AS El-Azab, Electrochemical behaviour and corrosion inhibition of Al, Al-6061 and Al–Cu in neutral aqueous solutions, Corros. Sci., 41 (1999), 709-727.

[74] Jin-Feng Li, Zhuo-wei Peng, Chao-Xing Li, Zhi-Qiang Jia, Wen-jing Chen, Zi-Qiao Zheng, Mechanical properties, corrosion behaviors and microstructures of 7075 aluminium alloy with various aging treatments, Transactions of Nonferrous Metals Society of China, 18 (2008), 755-762.

[75] BS Coving Jr, SD Cramer, JP Carter, David Schlain, Corrosion of titanium diboride, Journal of the Less Common Metals, 41 (1975), 211-224.

[76] DS Sekhawat, M Chakraborty, UK Chatterjee, Wear and Corrosion Behaviour of In-Situ Al-TiB_2 Metal Matrix Composites, Materials Science Forum, Trans Tech Publ, 2005, pp. 449-452.

[77] HH Sun, D Chen, XF Li, NH Ma, HW Wang, Electrochemical corrosion behavior of Al–Si alloy composites reinforced with in situ TiB2 particulate, Materials and corrosion, 60 (2009),

419-423.